Journal of Alloys and Compounds 860 (2021) 158446

Contents lists available at ScienceDirect

Journal of Alloys and Compounds

journal homepage: www.elsevier.com/locate/jalcom

Synthesis, characterization, and photocatalytic activity of stannum-doped $MgIn_2S_4$ microspheres

Wenhong Yang[a], Yujing Dong[b], Zhipeng Wang[a], Yuqin Li[a], Chunhui Dai[c], Dongwei Ma[b,*], Yu Jia[b], Zhen Yang[a,*], Chao Zeng[a,*]

[a] Institute of Advanced Materials, College of Chemistry and Chemical Engineering, Jiangxi Normal University, 99 Ziyang Avenue, Nanchang, Jiangxi Province 330022, China
[b] Key Laboratory for Special Functional Materials of Ministry of Education, and School of Materials Science and Engineering, Henan University, Kaifeng 475004, China
[c] Jiangxi Key Laboratory for Mass Spectrometry and Instrumentation, East China University of Technology, Nanchang 330013, China

ARTICLE INFO

Article history:
Received 13 October 2020
Received in revised form 19 December 2020
Accepted 21 December 2020
Available online 24 December 2020

Keywords:
Photocatalysis
CO_2 reduction
Sn
Doping
$MgIn_2S_4$

ABSTRACT

A series of Sn^{2+} doped $MgIn_2S_4$ photocatalysts were prepared via a facial hydrothermal method. The Sn dopants substitute the sites of Mg atom in $MgIn_2S_4$ unit cell, but not alter the crystal structure, demonstrated by the results of XRD and XPS. Compared to pristine $MgIn_2S_4$, Sn-doped $MgIn_2S_4$ samples exhibit significantly enhanced photocatalytic CO_2 reduction activity. With increasing the Sn dopant content, the CO_2 conversion rate first ascends, achieving the maximum rate at Sn-$MgIn_2S_4$-2 sample, and then decreases. After illumination for 4 h, the highest yield of CO and CH_4 for Sn-$MgIn_2S_4$-2 sample reaches about 3.35 and 3.33 times higher than that of pristine $MgIn_2S_4$. The theoretical results based on density functional theory calculations reveal that Sn doping in $MgIn_2S_4$ tunes the band structure from the direct-transition of $MgIn_2S_4$ to indirect-transition, diminishes band gap and extends the light absorption range, reduces the effective masses of holes and promotes the migration of photoinduced carriers. The experimental results also demonstrate the positive role of Sn dopant in accelerating the separation and transportation of charges, and improving CO_2 adsorption ability. This work systematically investigates and discusses the Sn^{2+} doping effect in $MgIn_2S_4$ on crystal structure, lattice variations, electronic band structures, CO_2 adsorption ability, and photocatalytic CO_2 reduction activity, which can provide a new hint for the fabrication of efficient photocatalyst by metal ion doping.

1. Introduction

Simultaneous solar energy conversion and storage via artificial photocatalytic process has arrested intensive interests in recent years [1]. The photocatalytic conversion of CO_2 into useful hydrocarbons is regarded as an eco-friendly strategy to settle the crisis of environmental issues and energy shortage [2]. However, this promising technology is hampered at the proof-of-concept stage because of the low CO_2 photoconversion efficiency [3]. The typical CO_2 photoreduction reaction generally involves three processes: photoabsorption, photoinduced charge carriers' separation and CO_2 reduction by photogenerated electrons [4]. The low photocatalytic CO_2 reduction activity can be ascribed to the following reasons: narrow scope of light absorption, high electron-hole recombination rate, sluggish kinetics for hydrocarbons evolution and so on [5–7]. Thus, developing visible-light-active photocatalyst with superior photoconversion efficiency is tempting and essential.

Ternary chalcogenide AB_2X_4 (A = Zn, Cd, Ca, Cu; B = In, Ga, Al; X = S, Se, Te) semiconductors, as potential visible-light-driven photocatalysts applied in various photocatalytic fields, has attracted intensive attention because of diverse outstanding characters, such as, unique and tunable electronic structure, excellent light-harvesting properties, and suitable energy level [8]. However, the isolated AB_2X_4 photocatalysts still suffer from the relatively high recombination rate of photoexcited carriers, resulting into the unsatisfactory photocatalytic performance [8–10]. To ameliorate the activity of photocatalysts, multifarious strategies have been exploited, such as morphology regulation, element doping, cocatalysts loading, utilizing exposed crystal facets, and heterogeneous coupling, and so on [11,12]. It is well-known that the carrier's

* Corresponding authors.
E-mail addresses: madw@henu.edu.cn (D. Ma), yangzhen@jxnu.edu.cn (Z. Yang), czeng@jxnu.edu.cn (C. Zeng).

https://doi.org/10.1016/j.jallcom.2020.158446
0925-8388/

transportation from bulk to surface reactive sites needs hundreds of picoseconds, while the recombination of electron-hole in the bulk of photocatalysts just takes several picoseconds, revealing that charge carriers are inclined to recombine rather than transfer to surface reactive sites [13,14]. The high bulk-charge recombination rate contributes significantly to the inefficient artificial photocatalysis system. Among the above-motioned modification methods of photocatalyst, it is the element doping that can boost the carrier separation and migration in the bulk, whilst the rest strategies just affect surface carrier transportation [15]. Zhao et al. reported that Cu-doped $ZnIn_2S_4$ exhibited enhanced photocatalytic hydrogen evolution under visible light irradiation [16]. Wang et al. synthesized Sn^{2+}-doped $ZnWO_4$ nanocrystals, which showed improved visible photocatalytic efficiency for methylene orange (MO) degradation [17]. Zhu et al. found that Sm-doped $ZnIn_2S_4$ microspheres would efficiently improve the photoactivity in the removal of methyl orange (MO) and Rhodamine B (RhB) [18]. In addition, other metal dopants, such as K^+ [19], Cu^{2+} [20], Y^{3+} [21], Ce^{3+} [22], and Mo^{5+} [23], doping in semiconductor photocatalysts, would also promote the photocatalytic properties.

$MgIn_2S_4$, a typical AB_2X_4 metal chalcogenide, has been reported and exhibited the photocatalytic activity in the photo-degradation of carbamazepine [24], methyl orange (MO) and 4-nitroaniline (4-NA) [8], the photoreduction of Cr (VI) and photocatalytic water splitting to hydrogen [25]. As mentioned earlier, element doping is an efficient strategy to enhance photocatalytic activity. Our group prepared carbon coating and doping $MgIn_2S_4$ with greatly enhanced photocatalytic CO_2 reduction activity, and the function of doped carbon and coated carbon in photocatalytic activity enhancement were investigated and discussed systematically [26]. Moreover, we also reported that Co surface gradient diffused doping in $MgIn_2S_4$ created an oriented built-in electric field, which could effectively extract photoinduced carriers from inner to surface, so inhibited charge recombination and enhanced photocatalysis performance for CO_2 reduction to CO [27]. However, the influence of metal ion homogeneous doping on the catalytic activity over $MgIn_2S_4$ might hold paramount importance in the understanding and designing of efficient photocatalysts, which has never been reported so far. In this work, a series of $MgIn_2S_4$ uniformly doped with different amounts of Sn^{2+} ions were synthesized via a facial hydrothermal method. The doping effect on crystal structure, lattice variations, electronic and band structures, CO_2 adsorption ability, and photocatalytic CO_2 reduction activity were systematically investigated and discussed.

2. Experimental section

2.1. Preparation of the photocatalyst

The reagents, $In(NO_3)_3{\cdot}xH_2O$, thioacetamide (TAA), $SnCl_2{\cdot}xH_2O$ were purchased from Shanghai Aladdin Bio-Chem Technology Co., LTD (Shanghai, China), and $MgIn_2S_4{\cdot}6H_2O$ was purchased from Sinopharm Chemical Reagent Co., Ltd. (Shanghai, China), all of which were of analytical grade and used without further purification. The Sn-doped $MgIn_2S_4$ microspheres were prepared by a simple hydrothermal method. Typically, $MgIn_2S_4{\cdot}6H_2O$, $SnCl_2{\cdot}xH_2O$, $In(NO_3)_3{\cdot}xH_2O$, and TAA were dissolved in 30 mL ultrapure water. After 30 min magnetic stirring, the resulting heterogeneous solution was transferred into a 50 mL Teflon-lined stainless-steel autoclave and maintained at 120 °C for 24 h in an oven. After natural cooling, the product was collected by centrifugation, washed alternately with distilled water and ethanol, and then dried at 60 °C for 10 h. For the convenient reason, the as-synthesized samples with $SnCl_2{\cdot}xH_2O$/$MgIn_2S_4{\cdot}6H_2O$ molar ratios of 10%, 20%, and 30% were named as Sn-$MgIn_2S_4$-1, Sn-$MgIn_2S_4$-2, and Sn-$MgIn_2S_4$-3, respectively. Moreover, the pure $MgIn_2S_4$ was synthesized by the same procedure without adding $SnCl_2{\cdot}xH_2O$.

2.2. Sample characterization

X-ray powder diffraction (XRD) were recorded on a Bruker D8 focus with Cu Kα radiation. X-ray photoelectron spectroscopy (XPS) was performed on an ESCALAB 250xi (ThermoFsher, England) electron spectrometer. Field emission scanning electron microscopy (FE-SEM) and transmission electron microscopy (TEM) was conducted on Hitachi SU8020 and JEM-2100, respectively. UV–vis diffuse reflectance spectra (DRS) were obtained using a Hitachi U-3310 UV–vis spectrophotometer. The Brunauer-Emmett-Teller (BET) specific surface area and pore diameter distribution of samples were measured through nitrogen adsorption-desorption on Micromeritics ASAP 2460 (USA). The CO_2 adsorption ability of as-obtained samples was investigated by An ASAP 2020 analyzer (Micromeritics, USA). The photoluminescence emission (PL) spectra were measured at a fluorescence spectrophotometer (Edinburgh FLS980) using xenon lamp as an excitation source. All the measurements were conducted at room temperature.

2.3. Photocatalytic CO_2 reduction test

The photocatalytic performance of as-prepared samples were evaluated by the photocatalytic CO_2 reduction experiment. Typically, 50 mg photocatalyst was ultrasonically dispersed in 90 mL ultrapure water and 10 mL TEOA (triethanolamine) used as sacrificial agent, and then the suspension was transferred into a 300 mL photoreactor sealed with an optical quartz window at the top. Before photoreaction, the reactor was first vacuumed, and then was continuously bubbled with high purity CO_2 gas (99.999%) for 30 min to get the saturated dissolution of CO_2 and adsorption-desorption equilibrium. The reactor internal pressure was 1 atm and the temperature was kept at room temperature by being cooled with circulating water to increase the solubility of CO_2. A 300 W Xe lamp was used as the light source. At certain period time, 0.2 mL resulting gas was collected by gas sampling needle and then qualitatively analyzed by a GC A60 gas chromatograph (Panna, Changzhou, TCD detector, FID detector, argon carrier gas). Blank test was conducted without photocatalyst, or without irradiation, or substitute CO_2 gas with nitrogen gas. The isotopic experiment in the presence of Sn-$MgIn_2S_4$-2 sample was performed under the same conditions with using $^{13}CO_2$ instead of $^{12}CO_2$. To assess the stability, Sn-$MgIn_2S_4$-2 sample taken as a model was reevaluated in the light of the aforementioned procedure.

2.4. Photoelectrochemical measurement

The photoelectrochemical measurements, including photocurrent response, electrochemical impedance spectra (EIS) and Mott-Schottky curve, were carried out on an electrochemical analyzer (CS315H, Wuhan) equipped with a standard three-electrode system. Platinum (Pt) wire and Ag/AgCl (saturated KCl) were used as the counter electrode and reference electrode, respectively. A 300 W Xe arc lamp was taken as light source. The electrolyte solution was 0.1 M Na_2SO_4 aqueous solution. The working electrodes was prepared as follows. 10 mg sample was ultrasonically dispersed in 800 μl ethanol. Then, the suspension liquid was drop-coated on an ITO glass with size of 20 mm × 40 mm, and dried at 60 ℃ for 10 h in the air.

2.5. Computational details

All the theoretical calculations were performed within the framework of density functional theory (DFT) using the plane-wave pseudopotential approach as implemented in the VASP code [28]. The generalized gradient approximation formulated by Perdew, Burke, and Ernzerhof (PBE) [29] as the exchange-correlation functional has been used for all the structure relaxations. According to

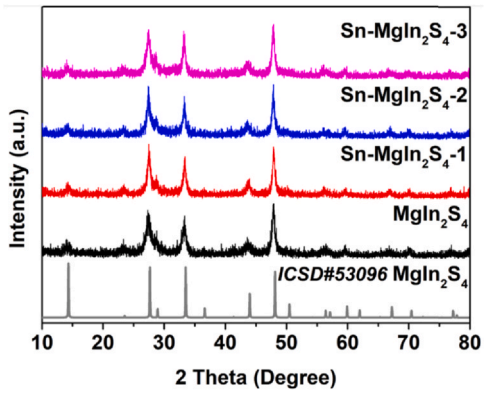

Fig. 1. XRD patterns of $MgIn_2S_4$ and Sn-$MgIn_2S_4$-2 samples.

the experimental results, the Sn-doped $MgIn_2S_4$ (Sn-$MgIn_2S_4$) has been modelled by replacing one Mg atom with one Sn atom in the unit cell, giving a doping concentration of 12.5% close to the experimental cases. The equilibrium structural parameters (including both lattice parameters and internal atomic coordinates) of each candidate material were obtained by the total energy minimization through the conjugate-gradient algorithm for $MgIn_2S_4$ and Sn-$MgIn_2S_4$. The kinetic energy cutoffs of 450 eV for the plane-wave basis set are used to ensure the residual forces on atoms converged to below 0.001 eV/Å. The 4 × 4 × 4 Monkhorst-Pack grids are adopted for structural optimization and densities of states (DOS) calculation. The effective masses of electrons (m_e^*) and holes (m_h^*) were calculated on the basis of the parabolic approximation of the conduction band minimum (CBM) and valence band maximum (VBM) [30]:

$$m^* = \pm \hbar^2 \left(\frac{d^2 E_k}{dk^2} \right)^{-1}$$

where k represents the wave-vector and E_k represents the energy corresponding to the wave vector k.

3. Results and discussion

The XRD patterns of $MgIn_2S_4$ and Sn-$MgIn_2S_4$-2 samples are displayed in Fig. 1. The main peaks of $MgIn_2S_4$ at 14.0°, 23.2°, 27.4°, 28.2°, 33.3°, 36.5°, 43.5°, 47.8°, 50.0°, 56.4°, 57.5°, 59.5°, 61.8°, 66.7°, 70.1°, 77.1°, and 77.5° coincide with (111), (022), (113), (222), (004), (133), (115), (044), (135), (335), (226), (444), (117), (137), (008), (555), and (266) planes of cubic $MgIn_2S_4$ (ICSD # 53096). No other impurities are detected, demonstrating the single-phase of $MgIn_2S_4$. All of the diffraction peaks for Sn-doped $MgIn_2S_4$ samples correspond well to the standard data of $MgIn_2S_4$, and no characteristic peaks of any impurities are observed in the patterns, reflecting that Sn dopant does not induce the alteration of crystal phase.

To investigate the chemical composition and chemical situation of the as-synthesized $MgIn_2S_4$ and Sn-$MgIn_2S_4$-2 samples, X-ray photoelectron spectroscopy (XPS) are carried out. The C 1s peak at 284.8 eV coming from adventitious carbon of the XPS instrument is employed to calibrate all binding energies. As shown in Fig. 2a, the $MgIn_2S_4$ is composed of Mg, In, S elements, and Sn-$MgIn_2S_4$-2 consists of Mg, In, S, Sn elements. The O 1s peak with bind energy of 529.3 eV is ascribed to the sample surface absorbed O_2 and H_2O [31]. For $MgIn_2S_4$, the peaks at 445.1 and 452.7 eV are ascribed to the In $3d_{5/2}$ and In $3d_{3/2}$ states of In^{3+} [32], while the In 3d peaks for Sn-$MgIn_2S_4$-2 sample are almost the same as $MgIn_2S_4$ (Fig. 2b). The binding energies of S^{2-} ions are 162.8 and 161.7 eV for $MgIn_2S_4$, 162.6 and 161.5 eV for Sn-$MgIn_2S_4$-2, which can be indexed to S $2p_{1/2}$ and S $2p_{3/2}$ (Fig. 2c), respectively [33]. It can be found from the crystal structure of $MgIn_2S_4$ in Fig. S7a and b that the S element is only bonded to Mg element. For Sn-$MgIn_2S_4$-2 sample, the negative shift of S 2p peaks and immobile In 3d peaks, in relative to that of $MgIn_2S_4$, demonstrate that the Sn dopants substitute the sites of Mg atoms. If the doped Sn exists in an interstitial configuration, the

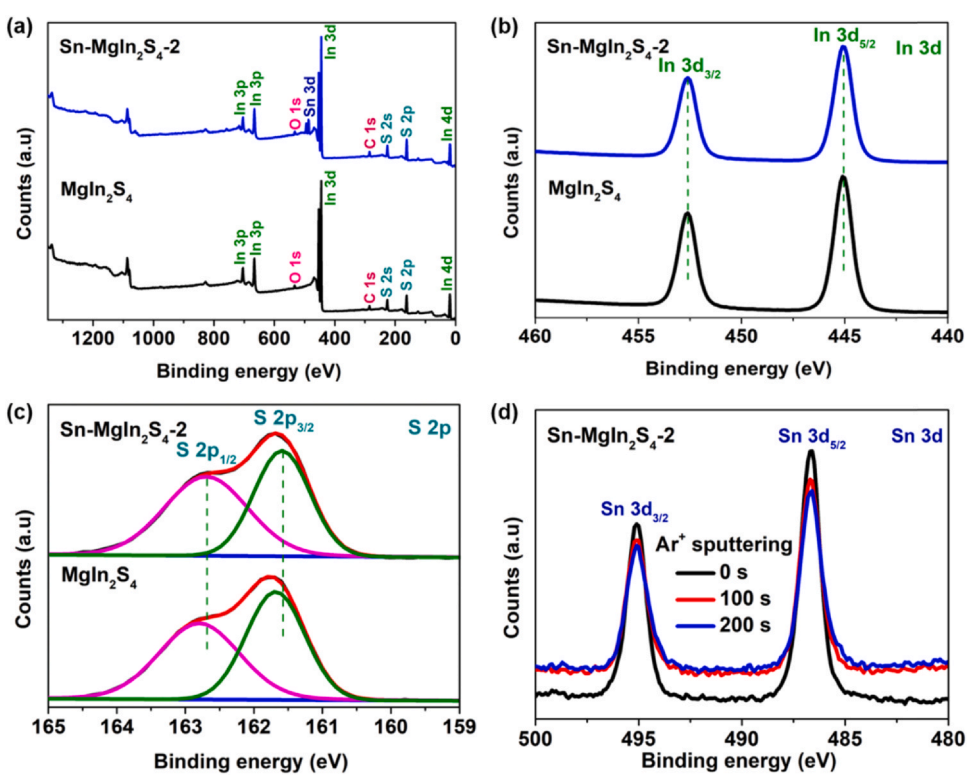

Fig. 2. Typical XPS survey spectra (a), high-resolution XPS spectra of In (b) and S (c) for $MgIn_2S_4$ and Sn-$MgIn_2S_4$-2 samples. Time-dependent high-resolution Sn 3d XPS spectra upon Ar^+ sputtering for Sn-$MgIn_2S_4$-2 sample (d).

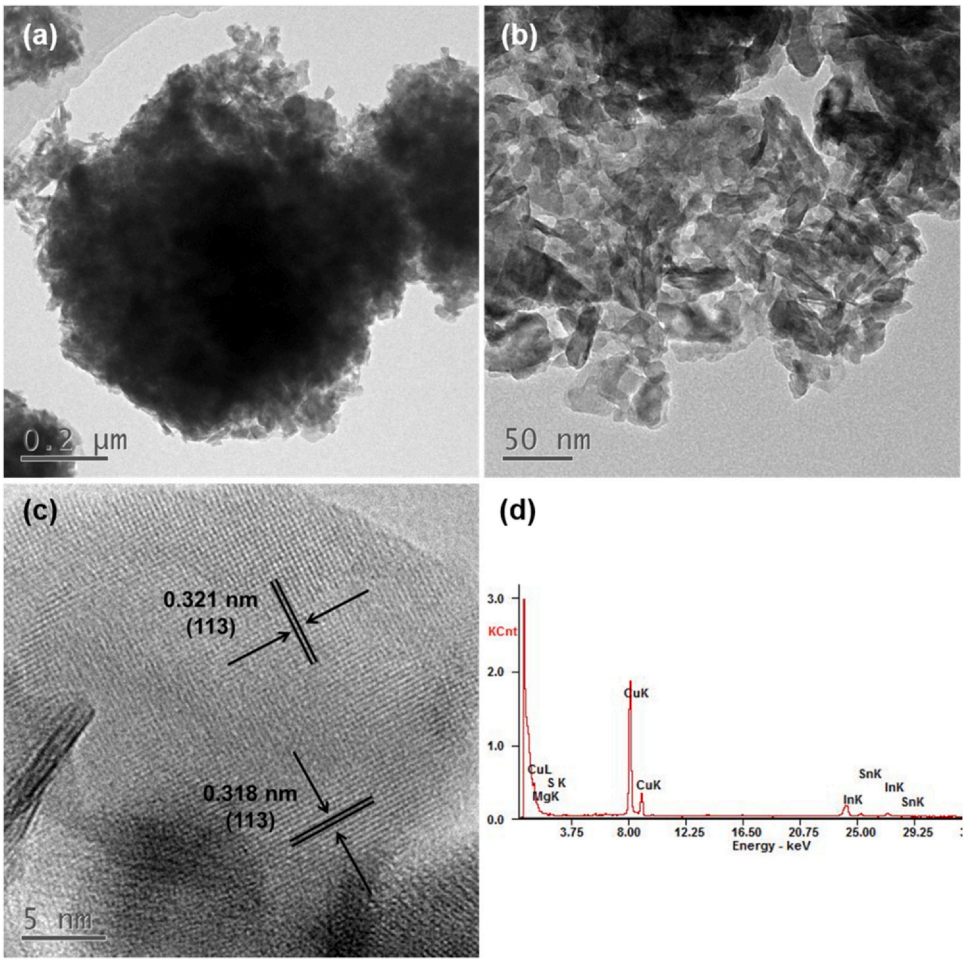

Fig. 3. TEM image (a-b), HRTEM image (c), and EDX spectrum (d) for Sn-$MgIn_2S_4$-2 sample.

electron density of both In atoms and S atoms would be changed, and the bind energy of In element would be changed [34]. To investigate the distribution of Sn dopants in the bulk and subsurface of Sn-$MgIn_2S_4$-2 sample, time-dependent high-resolution Sn 3d XPS spectra upon Ar^+ sputtering are performed. After Ar^+ sputtering for 100 s, the peak intensity of Sn 3d remains unchanged with prolong the sputtering time [35]. Therefore, the Sn^{2+} ions are successfully introduced into the unit cell of $MgIn_2S_4$ rather than absorbed on the surface or forms surface gradient diffused doping.

The morphology and microstructure of the as-synthesized samples are investigated by SEM, TEM, HRTEM, and TEM-EDX, as exhibited in Fig. 3 and Figs. S1–2. From Fig. S1, it can be seen that the $MgIn_2S_4$ is characterized by microsphere composed of nanosheets. The introduction of Sn dopant has not made an obvious difference to the morphology of $MgIn_2S_4$. The TEM images in Fig. 3a and b and Fig. S2 further confirm that the microsphere of as-prepared sample is an aggregation of nanosheets. For the HRTEM image in Fig. 3c, Sn-$MgIn_2S_4$-2 sample displays clear lattice fringes with lattice plane spacing of 0.321 nm and 0.318 nm, which can be contributed to the typical (113) facets. The result of TEM-EDX reflects the existence of Mg, Sn, In, and S atoms (Fig. 3d).

The photocatalytic activities of as-prepared samples were evaluated by the photocatalytic CO_2 reduction experiment. As shown in Fig. 4a, CO_2 can be photo-reduced to CO and CH_4 in the presence of $MgIn_2S_4$ and Sn-$MgIn_2S_4$ samples. The Sn-$MgIn_2S_4$ samples exhibit markedly enhanced photocatalytic CO_2 reduction activity compared with pristine $MgIn_2S_4$. With enlarging the content of Sn dopant, the CO_2 conversion rate first ascends, achieving the maximum rate at Sn-$MgIn_2S_4$-2 sample, and then decrease because excess metal ion dopant would act as the center of electron-hole recombination [27]. After illumination for 4 h, the highest yield of CO and CH_4 is 1.70 and 0.13 umol/g, which is about 3.35 and 3.33 times higher than that of pristine $MgIn_2S_4$ (the yield of CO and CH_4 is 0.39 and 0.03 umol/g), respectively. The Table S1 portrays the performance comparison of different photocatalysts for photocatalytic CO_2 reduction. To verify the selectivity of product formation from CO_2 reduction over Sn-$MgIn_2S_4$-2 sample by using other scavenger, we conduct the photocatalytic CO_2 reduction experiment under the same conditions just substituting triethylamine for TEOA, and the time dependence of CH_4 and CO yields for photo-reduction of CO_2 over Sn-$MgIn_2S_4$-2 sample is shown in Fig. S4. The products using triethylamine as scavenger are CO and CH_4, while the yield of CO is lower than that using TEOA as scavenger, but the yield of CH_4 is higher than that using TEOA as scavenger. Particularly, in the blank experiments, neither CO or CH_4 is produced and detected without photocatalyst, or without irradiation, or substitute CO_2 gas with nitrogen gas. Furthermore, as corroborated by the isotopic experiment using $^{13}CO_2$ instead of $^{12}CO_2$ (Fig. 4b), the *m/z* at 45, 17, and 29 on the GC-MS spectra can be attributed to $^{13}CO_2$, $^{13}CH_4$, and ^{13}CO, respectively. Thus, it can be confirmed that the CO and CH_4 are derived from the photocatalytic CO_2 reduction reaction over Sn-$MgIn_2S_4$-2 sample, rather than the decomposition of any organic impurity.

Besides the photocatalytic CO_2 reduction activity of semiconductor photocatalysts, the stability and recyclability are also pivotal for practical applications, which is evaluated by conducting three-run cycling CO_2 photoreduction experiments. After three successive cycles, as

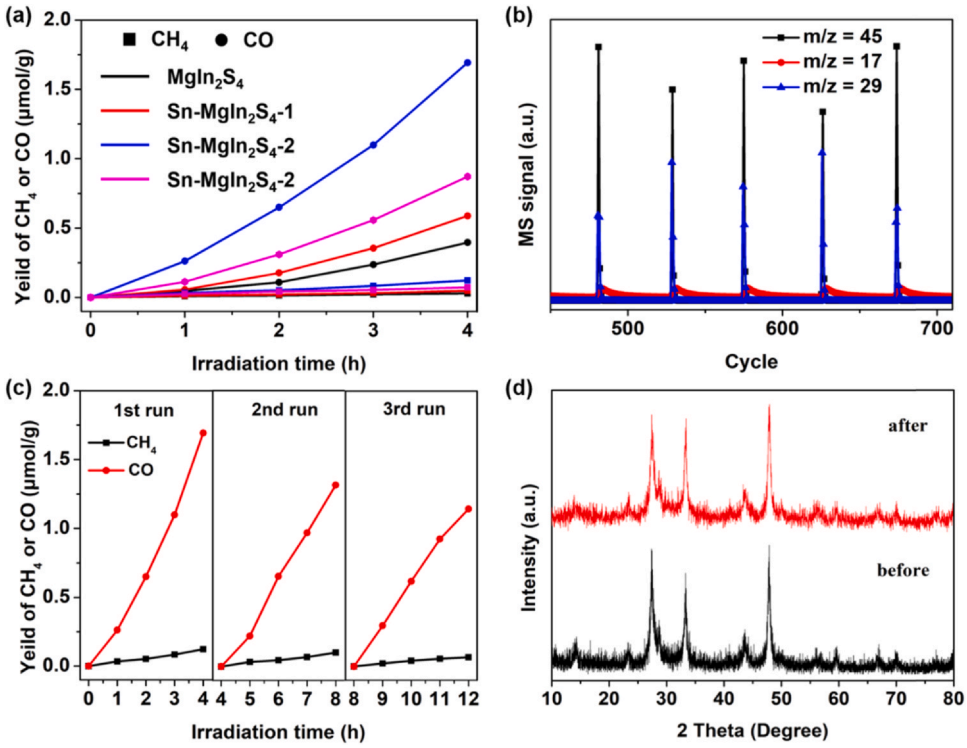

Fig. 4. (a) Time dependence of CH_4 and CO yields for photo-reduction of CO_2 over $MgIn_2S_4$ and Sn-$MgIn_2S_4$ samples. (b) Mass spectra for CO_2 reduction over Sn-$MgIn_2S_4$-2 sample under $^{13}CO_2$ atmosphere. Cycling runs of CO_2 reduction over Sn-$MgIn_2S_4$-2 sample (c). XRD pattern of Sn-$MgIn_2S_4$-2 sample before and after photocatalytic reaction (d).

shown in Fig. 4c, the Sn-MgIn2S4-2 sample maintains over 60% of its photocatalytic activity in photo-reducing CO_2 to generate both CO and CH_4. In addition, it can be found from Fig. 4d and Fig. S5 that no obvious variations of XRD pattern and SEM image for Sn-$MgIn_2S_4$-2 sample between before and after photoreaction can be detected. These results imply the favorable photostability of Sn-$MgIn_2S_4$-2 sample, which is beneficial for its potential practical application.

The specific surface areas (S_{BET}) of $MgIn_2S_4$ and Sn-$MgIn_2S_4$-2 samples are determined to be 73.9 and 40.1 m^2/g based on the Brunauer-Emmett-Teller (BET) method (Fig. S6). Generally, a higher surface area of semiconductor photocatalysts implies the more active sites exposed for CO_2 adsorption and photocatalytic CO_2 reduction reaction, which is be advantageous for the photocatalysis performance [36]. Although the S_{BET} of Sn-$MgIn_2S_4$-2 is smaller than that of $MgIn_2S_4$, the enhanced photocatalytic activity of Sn-$MgIn_2S_4$-2 do reveal the important positive effect of Sn dopant. We also measure the CO_2 adsorption ability of $MgIn_2S_4$ and Sn-$MgIn_2S_4$-2 samples, which is crucial for the photocatalytic CO_2 reduction to hydrocarbons [26]. As shown in Fig. 5a, the introduction of Sn dopant would strengthen the CO_2 adsorption capacity. Moreover, during the photocatalytic CO_2 reduction reaction, water serve as the electron donor and a proton source, suggesting that the contact degree between photocatalyst and water has an impact on the CO_2 photoconversion efficiency [37]. The static water contact-angle measurement of $MgIn_2S_4$ and Sn-$MgIn_2S_4$-2 samples are examined, as exhibited in Fig. S7. It can be found that the contact angle of these two samples is not significantly different, so the contact degree is not the cause of the enhancement for photocatalytic activity.

The separation and migration efficiency of photo-generate charges are critical to the photocatalysis performance over semiconductor photocatalysts. The EIS Nynquist plots, transient photocurrent responses, and PL spectra of $MgIn_2S_4$ and Sn-$MgIn_2S_4$-2 samples are measured and displayed in Fig. 5b-d. For EIS Nynquist plots (Fig. 5b), the sharply reduced arc radius of Sn-$MgIn_2S_4$-2 compared with $MgIn_2S_4$ can be detected. In general, the smaller EIS Nynquist plots is, the higher charge transfer efficiency is [38]. The Sn-$MgIn_2S_4$-2 sample exhibits a remarkable enhanced current density in relative to that of $MgIn_2S_4$ (Fig. 5c), while the higher current density represents a better charge separation efficiency [39]. The photoluminescence emission (PL) intensity of Sn-$MgIn_2S_4$-2 is lower than that of $MgIn_2S_4$ (Fig. 5d), demonstrating a lower charge recombination rate over Sn-$MgIn_2S_4$-2 [40]. According to the above measurement results, it can be inferred that Sn^{2+} doping in $MgIn_2S_4$ can effectively promote the separation and transportation efficiency of photogenerated carriers, so enhancing photocatalytic CO_2 reduction activity.

DFT calculations are carried out to try to understand how the Sn dopants alter the photocatalytic performance of $MgIn_2S_4$. In the light of the XPS results (Fig. 2), the Sn-doped $MgIn_2S_4$ is modelled by replacing one Mg atom with one Sn atom in the unit cell, as shown in Fig. 6a and b. Table. S2 exhibits that Sn doping has little effect on the structure of $MgIn_2S_4$, and the lattice parameter increases slightly from 10.90 Å for $MgIn_2S_4$ to 10.97 Å for Sn-$MgIn_2S_4$, which is due to the larger atomic radius of Sn elements. The main factors affecting the photocatalytic conversion efficiency are the light absorption range of photocatalytic materials and the separation and utilization efficiency of photogenerated carriers. The band structure results exhibit that Sn-$MgIn_2S_4$ has a narrower bandgap (0.69 eV) than $MgIn_2S_4$ (1.74 eV) (Fig. 6c and Fig. S8c), and noticeably, the band structure changes from the direct band gap to indirect band gap. For indirect band materials, the momentum between the CBM and VBM is mismatch. The recombination between electrons and holes must conserve momentum, so, for semiconductor photocatalyst, the indirect-transition of band structure can significantly reduce charge recombination rate compared with the direct-transition of band structure [41]. Sn doping increase the dispersion of the contour distribution of VBM and CBM, suggesting Sn doping promotes the charge mobility [42]. A narrow band gap can improve the light absorption and affect both the electron delocalization and mobility of the photoexcited charge, which significantly affect the photocatalytic efficiency [43]. Comparing the DOS of the simulated $MgIn_2S_4$ and Sn-$MgIn_2S_4$ systems, for $MgIn_2S_4$,

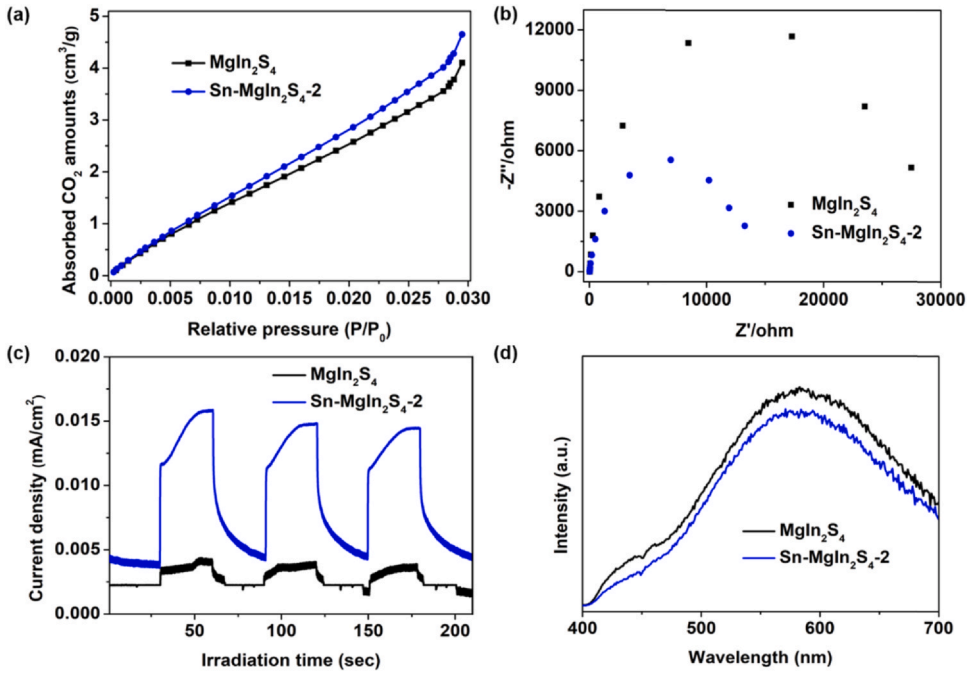

Fig. 5. CO_2 adsorption curves (a), EIS Nynquist plots (b), transient photocurrent responses (c), and PL spectra (d) of $MgIn_2S_4$ and Sn-$MgIn_2S_4$-2 samples.

the CB and VB are mainly composed of In (s) + S (p), and In (p) + S (p), respectively. For Sn-$MgIn_2S_4$, the CB and VB are mainly composed of In (s) + S (p), and Sn (s) + S (p), respectively (Fig. 6d and Fig. S8d).

The indirect bandgap can reduce the recombination of electrons and holes and make Sn-$MgIn_2S_4$ samples show the improved photocatalytic activity. In order to further study the charge separation and transport characteristics, the effective masses of electrons and holes of $MgIn_2S_4$ and Sn-$MgIn_2S_4$ are calculated and analyzed. The effective masses of electrons and holes for $MgIn_2S_4$ are $m^*_e = 0.48\ m_0$ and $m^*_h = 6.87\ m_0$, respectively, and those for

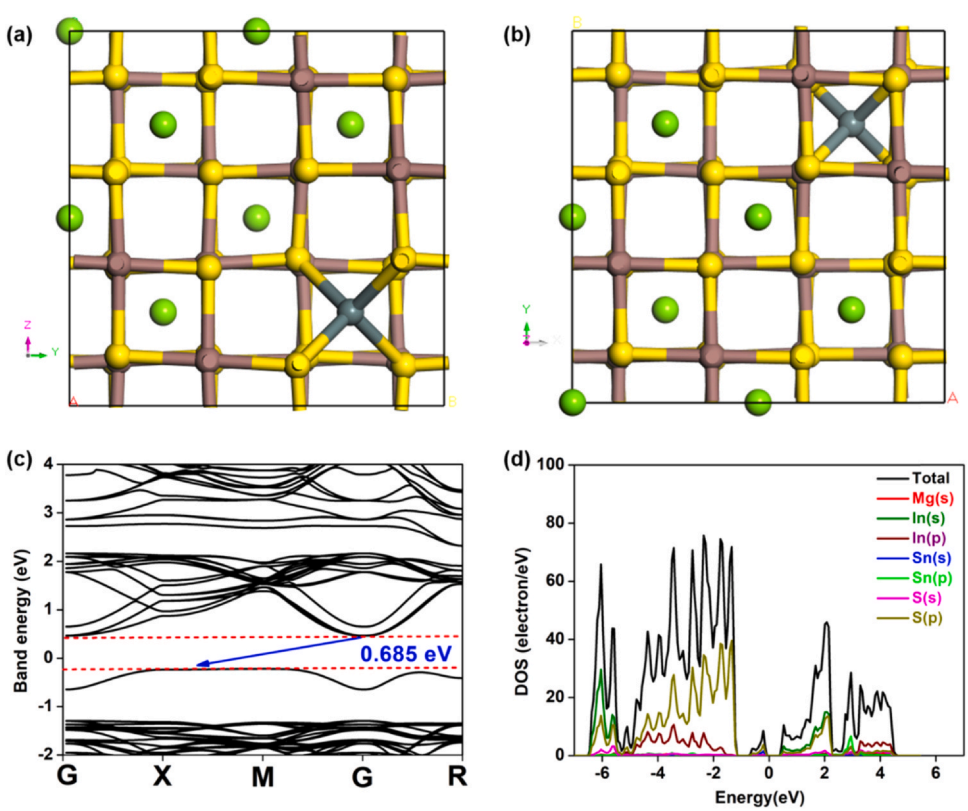

Fig. 6. Side (a) and top (b) views of model structure for Sn-$MgIn_2S_4$. Electronic band structure (c) and density of state (d) of the simulated Sn-$MgIn_2S_4$ system. The green, brown, yellow and grey atoms represented Mg, In, S, and Sn atoms, respectively. (For interpretation of the references to colour in this figure legend, the reader is referred to the web version of this article.)

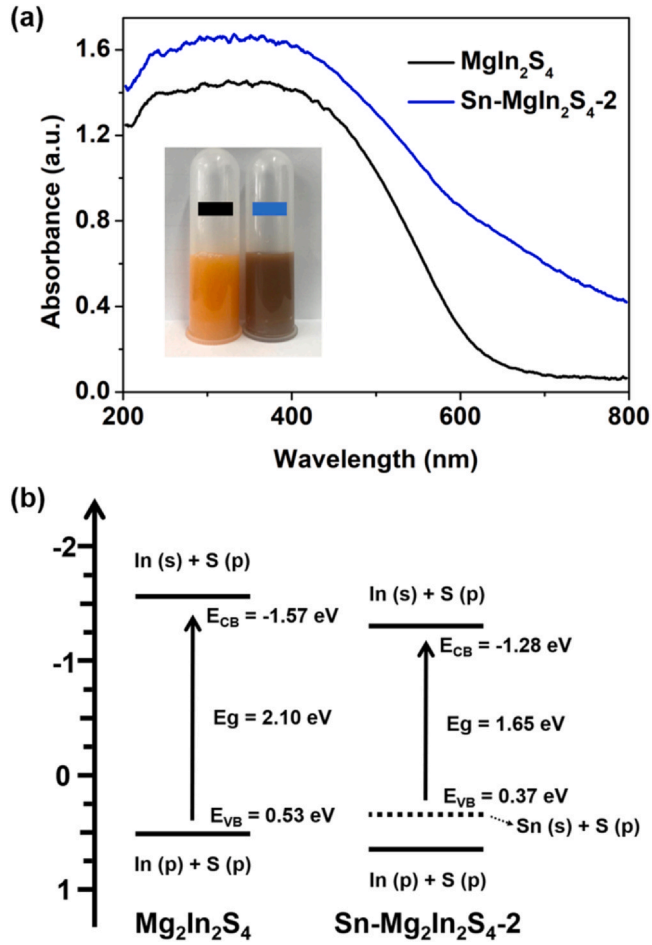

Fig. 7. (a) DRS spectra and digital photo of suspensions in the inset of $MgIn_2S_4$ and Sn-$MgIn_2S_4$-2 samples. (b) Schematic band structures for $MgIn_2S_4$ and Sn-$MgIn_2S_4$-2 samples. (For interpretation of the references to colour in this figure legend, the reader is referred to the web version of this article.)

Sn-$MgIn_2S_4$ are $m^*_e = 0.68\ m_0$ and $m^*_h = 5.09\ m_0$, respectively. Large m^* reflects poor mobility of photoinduced carriers [44]. The effective masse of holes is much larger than those of electrons for both the pristine and the doped samples, and thus the mobility of photoinduced carriers is primarily determined by the mobility of holes. The m^*_h of Sn-$MgIn_2S_4$ is significantly reduced compared to that of $MgIn_2S_4$, so the migration of photoinduced carriers is greatly promoted.

Fig. 7a shows the DRS spectra and digital photo of suspensions of $MgIn_2S_4$ and Sn-$MgIn_2S_4$ sample. The introduction of Sn dopant can effectively extend the light absorption range, which is consistent to the color change from red (color of pristine $MgIn_2S_4$) to dark brown (color of Sn-$MgIn_2S_4$), and induce the generation of a tail in the edge, which keeps in line with the result of theoretical results in Fig. 6d. Because Sn doping in $MgIn_2S_4$ causes the band structure changes from the direct band gap to indirect band gap, the energy band gap (Eg) of $MgIn_2S_4$ and Sn-$MgIn_2S_4$-2 are determined to be 2.10 and 1.65 eV (Fig. S9) on the basis of Kubelka-Munk equation, respectively. The experimental Eg calculated from DRS spectra is a bit bigger than that of theoretical value, the error of which is normal because of the limitation for the exchange-correlation potentials [45]. On the basis of Mott-Schottky curve in Fig. S10, the CB potential of $MgIn_2S_4$ and Sn-$MgIn_2S_4$-2 samples are calculated to be − 1.67 and − 1.38 eV versus Ag/AgCl, which are equal to − 1.57, and − 1.28 V versus the normal hydrogen electrode (NHE), so the VB potential can be determined to be 0.53 and 0.37 eV, respectively, as portrayed in Fig. 7b. As shown in Fig. S11, XPS valence band spectra of $MgIn_2S_4$ and Sn-$MgIn_2S_4$-2 samples are conducted to investigate the band edges, and the VB XPS values are determined to be 1.67 and 1.59 eV, the order of which coincides with the VB potential calculated above. Both the CB potentials of $MgIn_2S_4$ and Sn-$MgIn_2S_4$-2 samples meet the thermodynamic requirements of the CO_2 reduction into CH_4 and CO reaction: $CO_2 + 8H^+ + 8e^- \rightarrow CH_4 + 2H_2O$ (the reaction potential is −0.24 V VS NHE), $CO_2 + 2H^+ + 2e^- \rightarrow CO + H_2O$ (the reaction potential is −0.53 V VS NHE), respectively. The CO evolution during the photocatalytic CO_2 reduction reaction over $MgIn_2S_4$ and Sn-$MgIn_2S_4$-2 samples are higher than CH_4 evolution, which may be ascribed to the easily occur for double electron reaction, and the same phenomenon has also been reported [46–48]. Electrons and holes would be produced with irradiation and transfer to the photocatalytic surface reactive site. CO_2 would be reduced by electrons to be CH_4 and CO, while the TEOA would be oxidized by holes to generates C1 products as well as H_2 [49].

4. Conclusions

In summary, we confirm that metal ion doping is a feasible strategy to alter the electronic and band structures for semiconductor photocatalysts and thus remarkedly promotes their photocatalysis performance with taking $MgIn_2S_4$ as the model. Sn^{2+} doped $MgIn_2S_4$ photocatalysts exhibits greatly enhanced photocatalytic CO_2 reduction activity in relative to pristine $MgIn_2S_4$. Sn-$MgIn_2S_4$-2 sample realize the highest CO_2 photoconversion rate among all of the samples. With further enlarging the content of Sn dopant, the photocatalytic activities of Sn-doped $MgIn_2S_4$ samples declines, revealing the existence of optimal amount for metal ion doping. The theoretical calculation and experimental results demonstrate that the enhancement of photocatalytic activity for Sn-doped $MgIn_2S_4$ photocatalysts is ascribed to the promoted separation and transportation efficiency of photoinduced charges, strengthened CO_2 adsorption ability, and expanded light absorption range resulting from Sn doping. This study supports that metal ion doping strategy is attractive for the designing and fabrication of efficient semiconductor photocatalyst.

CRediT authorship contribution statement

Wenhong Yang: Investigation, Writing. **Yujing Dong:** Software. **Zhipeng Wang:** Data curation. **Yuqin Li:** Visualization. **Chunhui Dai:** Methodology. **Dongwei Ma:** Investigation, Software. **Yu Jia:** Software. **Zhen Yang:** Data curation, Resources. **Chao Zeng:** Conceptualization, Methodology, Software, Writing - review & editing.

Declaration of competing interest

The authors declare that they have no known competing financial interests or personal relationships that could have appeared to influence the work reported in this paper.

Acknowledgement

This work was supported by the National Natural Science Foundation of China (No. 51872130, 52063016, 52002158, 2652015296, 21968009), the Natural Science Foundation of Jiangxi Province (No. 20202BAB214009, 20202BAB203007), and the Education Department of Jiangxi Province (No. GJJ191684). No conflict of interest exists in this work.

Appendix A. Supporting information

Supplementary data associated with this article can be found in the online version at doi:10.1016/j.jallcom.2020.158446.

References

[1] X. Li, J.G. Yu, M. Jaroniec, X.B. Chen, Cocatalysts for selective photoreduction of CO_2 into solar fuels, Chem. Rev. 119 (2019) 3962–4179.
[2] J.K. Stolarczyk, S. Bhattacharyya, L. Polavarapu, J. Feldmann, Challenges and prospects in solar water splitting and CO_2 reduction with inorganic and hybrid nanostructures, ACS Catal. 8 (2018) 3602–3635.
[3] X.X. Chang, T. Wang, J.L. Gong, CO_2 photo-reduction: insights into CO_2 activation and reaction on surfaces of photocatalysts, Energy Environ. Sci. 9 (2016) 2177–2196.
[4] X.D. Li, Y.F. Sun, J.Q. Xu, Y.J. Shao, J. Wu, X.L. Xu, Y. Pan, H.X. Ju, J.F. Zhu, Y. Xie, Selective visible-light-driven photocatalytic CO_2 reduction to CH_4 mediated by atomically thin $CuIn_5S_8$ layers, Nat. Energy 4 (2019) 690–699.
[5] S.B. Wang, Y. Wang, S.Q. Zang, X.W. Lou, Hierarchical hollow heterostructures for photocatalytic CO_2 reduction and water splitting, Small Methods 4 (2020) 1900586.
[6] W.G. Tu, Y. Zhou, Z.G. Zou, Photocatalytic conversion of CO_2 into renewable hydrocarbon fuels: state-of-he-art accomplishment, challenges, and prospects, Adv. Mater. 26 (2014) 4607–4626.
[7] J.K. Stolarczyk, S. Bhattacharyya, L. Polavarapu, J. Feldmann, Challenges and prospects in solar water splitting and CO_2 reduction with inorganic and hybrid nanostructures, ACS Catal. 8 (2018) 3602–3635.
[8] W. Chen, Y.X. Hua, Y. Wang, T. Huang, T.Y. Liu, X.H. Liu, Two-dimensional mesoporous g-C_3N_4 nanosheet-supported $MgIn_2S_4$ nanoplates as visible-light-active heterostructures for enhanced photocatalytic activity, J. Catal. 349 (2017) 8–18.
[9] J. Chen, H. Zhang, P. Liu, Y. Li, X. Liu, G. Li, P.K. Wong, T. An, H. Zhao, Crosslinked $ZnIn_2S_4$/rGO composite photocatalyst for sunlight-driven photocatalytic degradation of 4-nitrophenol, Appl. Catal. B Environ. 168–169 (2015) 266–273.
[10] W.-K. Jo, T.S. Natarajan, Facile synthesis of novel redox-mediator-free direct Z-scheme $CaIn_2S_4$ marigold-flower-like/TiO_2 photocatalysts with superior photocatalytic efficiency, ACS Appl. Mater. Interfaces 7 (2015) 17138–17154.
[11] L.M. Wang, W.L. Chen, D.D. Zhang, Y.P. Du, R. Amal, S.Z. Qiao, J.B. Wu, Z.Y. Yin, Surface strategies for catalytic CO_2 reduction: from two-dimensional materials to nanoclusters to single atoms, Chem. Soc. Rev. 48 (2019) 5310–5349.
[12] K. Li, B.S. Peng, T.Y. Peng, Recent advances in heterogeneous photocatalytic CO_2 conversion to solar fuels, ACS Catal. 6 (2016) 7485–7527.
[13] J. Schneider, M. Matsuoka, M. Takeuchi, J.L. Zhang, Y. Horiuchi, M. Anpo, D.W. Bahnemann, Understanding TiO_2 photocatalysis: mechanisms and materials, Chem. Rev. 114 (2014) 9919–9986.
[14] Z.J. Zhang, W.Z. Wang, E.P. Gao, M. Shang, J.H. Xu, Enhanced photocatalytic activity of Bi_2WO_6 with oxygen vacancies by zirconium doping, J. Hazard. Mater. 196 (2011) 255–262.
[15] J. Li, L.J. Cai, J. Shang, Y. Yu, L.Z. Zhang, Giant enhancement of internal electric field boosting bulk charge separation for photocatalysis, Adv. Mater. 28 (2016) 4059–4064.
[16] S.H. Shen, L. Zhao, Z.H. Zhou, L.J. Guo, Enhanced photocatalytic hydrogen evolution over Cu-doped $ZnIn_2S_4$ under visible light irradiation, J. Phys. Chem. C 112 (2008) 16148–16155.
[17] Y.G. Su, B.L. Zhu, K. Guan, S.S. Gao, L. Lv, C.F. Du, L.M. Peng, L.C. Hou, X.J. Wang, Particle size and structural control of $ZnWO_4$ nanocrystals via Sn^{2+} doping for tunable optical and visible photocatalytic properties, J. Phys. Chem. C 116 (2012) 8508–18517.
[18] C.W. Tan, G.Q. Zhu, M. Hojamberdiev, K.S. Lokesh, X.C. Luo, L. Jin, J.P. Zhou, P. Liu, Adsorption and enhanced photocatalytic activity of the {0 0 0 1} faceted Sm-doped $ZnIn_2S_4$ microspheres, J. Hazard. Mater. 278 (2014) 572–583.
[19] T. Xiong, W.L. Cen, Y.X. Zhang, F. Dong, Bridging the g-C_3N_4 interlayers for enhanced photocatalysis, ACS Catal. 6 (2016) 2462–2472.
[20] M. Wang, M. Shen, X.X. Jin, J.J. Tian, M.L. Li, Y.J. Zhou, L.X. Zhang, Y.S. Li, J.L. Shi, Oxygen vacancy generation and stabilization in CeO_{2-x} by Cu introduction with improved CO_2 photocatalytic reduction activity, ACS Catal. 9 (2019) 4573–4581.
[21] A.D. Liyanage, S.D. Perera, K. Tan, Y. Chabal, K.J. Balkus Jr., Synthesis characterization, and photocatalytic activity of Y-doped CeO_2 nanorods, ACS Catal. 4 (2014) 577–584.
[22] Z. Dai, F. Qin, H.P. Zhao, J. Ding, Y.L. Liu, R. Chen, Crystal defect engineering of aurivillius Bi_2MoO_6 by Ce doping for increased reactive species production in photocatalysis, ACS Catal. 6 (2016) 3180–3192.
[23] N. Zhang, A. Jalil, D.X. Wu, S.M. Chen, Y.F. Liu, C. Gao, W. Ye, Z.M. Qi, H.X. Ju, C.M. Wang, X.J. Wu, L. Song, J.F. Zhu, Y.J. Xiong, Refining defect states in $W_{18}O_{49}$ by Mo doping: a strategy for tuning N_2 activation towards solar-driven nitrogen fixation, J. Am. Chem. Soc. 140 (2018) 9434–9443.
[24] Y. Guo, Y.H. Ao, P.F. Wang, C. Wang, Mediator-free direct dual-Z-scheme Bi_2S_3/$BiVO_4$/$MgIn_2S_4$ composite photocatalysts with enhanced visible-light-driven performance towards carbamazepine degradation, Appl. Catal. B Environ. 254 (2019) 479–490.
[25] L.Q. Jing, Y.G. Xu, M. Xie, J. Liu, J.J. Deng, L.Y. Huang, H. Xu, H.M. Li, Three dimensional polyaniline/$MgIn_2S_4$ nanoflower photocatalysts accelerated interfacial charge transfer for the photoreduction of Cr(VI), photodegradation of organic pollution and photocatalytic H_2 production, Chem. Eng. J. 360 (2019) 1601–1612.
[26] C. Zeng, Q. Zeng, C.H. Dai, L.K. Zhang, Y.M. Hu, Synergistic effect of surface coated and bulk doped carbon on enhancing photocatalytic CO_2 reduction for $MgIn_2S_4$ microflowers, Appl. Surf. Sci. 542 (2021) 148686.
[27] C. Zeng, Q. Zeng, C.H. Dai, Y.M. Hu, An oriented built-in electric field induced by cobalt surface gradient diffused doping in $MgIn_2S_4$ for enhanced photocatalytic CH_4 evolution, Dalton Trans. 49 (2020) 9213–9217.
[28] G. Kresse, J. Furthmüller, Efficient iterative schemes for ab initio total-energy calculations using a plane-wave basis set, Phys. Rev. B 54 (1996) 11169–11186.
[29] J.P. Perdew, K. Burke, M. Ernzerhof, Generalized gradient approximation made simple, Phys. Rev. Lett. 77 (1996) 3865–3868.
[30] M.M. Li, Y. Dai, X.C. Ma, Z.J. Li, B.B. Huang, The synergistic effect between effective mass and built-in electric field for the transfer of carriers in nonlinear optical materials, Phys. Chem. Chem. Phys. 17 (2015) 17710–17717.
[31] J.N. Feng, Z.Q. Yang, S. He, X.J. Niu, T.P. Zhang, A. Ding, H. Liang, X.C. Feng, Photocatalytic reduction of Uranium(VI) under visible light with Sn-doped In_2S_3 microspheres, Chemosphere 212 (2018) 114–123.
[32] D.L. Jiang, J. Li, C.S. Xing, Z.Y. Zhang, S.C. Meng, M. Chen, Two-dimensional $CaIn_2S_4$/g-C_3N_4 heterojunction nanocomposite with enhanced visible-light photocatalytic activities: interfacial engineering and mechanism insight, ACS Appl. Mater. Interfaces 7 (2015) 19234–19242.
[33] M. Zhou, S.B. Wang, P.J. Yang, C.J. Huang, X.C. Wang, Boron carbon nitride semiconductors decorated with CdS nanoparticles for photocatalytic reduction of CO_2, ACS Catal. 8 (2018) 4928–4936.
[34] C. Zeng, Y.M. Hu, T.R. Zhang, F. Dong, Y.H. Zhang, H.W. Huang, A core–satellite structured Z-scheme catalyst $Cd_{0.5}Zn_{0.5}S$/$BiVO_4$ for highly efficient and stable photocatalytic water splitting, J. Mater. Chem. A 6 (2018) 16932–16942.
[35] Y.J. Sun, T. Xiong, F. Dong, H.W. Huang, W.L. Cen, Interlayer-I-doped BiOIO3 nanoplates with optimized electronic structure for efficient visible light photocatalysis, Chem. Commun. 52 (2016) 8243–8246.
[36] I. Shown, S. Samireddi, Y.C. Chang, R. Putikam, P.H. Chang, A. Sabbah, F.Y. Fu, W.F. Chen, C.I. Wu, T.Y. Yu, P.W. Chung, M.C. Lin, L.C. Chen, K.H. Chen, Carbon-doped SnS_2 nanostructure as a highefficiency solar fuel catalyst under visible light, Nat. Commun. 9 (2018) 169.
[37] X.C. Jiao, Z.W. Chen, X.D. Li, Y.F. Sun, S. Gao, W.S. Yan, C.M. Wang, Q. Zhang, Y. Lin, Y. Luo, Y. Xie, Defect-mediated electron-hole separation in one-unit-cell $ZnIn_2S_4$ layers for boosted solar-driven CO_2 reduction, J. Am. Chem. Soc. 139 (2017) 7586–7594.
[38] J.Y. Li, X. Yu, Y. Zhu, X.H. Fu, Y.M. Zhang, 3D-2D-3D BiOI/porous g-C_3N_4/graphene hydrogel composite photocatalyst with synergy of adsorption-photocatalysis in static and flow systems, J. Alloy. Compd. 850 (2021) 156778.
[39] A. Uddin, T. Muhmood, Z.C. Guo, J.Y. Gu, H. Chen, F. Jiang, Hydrothermal synthesis of 3D/2D heterojunctions of $ZnIn_2S_4$/oxygen doped g-C_3N_4 nanosheet for visible light driven photocatalysis of 2,4-dichlorophenoxyacetic acid degradation, J. Alloy. Compd. 845 (2020) 156206.
[40] F.T. Yi, J.Q. Ma, C.W. Lin, L.Y. Wang, H.N. Zhang, Y.X. Qian, K.F. Zhang, Insights into the enhanced adsorption/photocatalysis mechanism of a $Bi_4O_5Br_2$/g-C_3N_4 nanosheet, J. Alloy. Compd. 821 (2020) 153557.
[41] X. Zhang, J.X. Shen, W.N. Wang, C.G. Walle, First-principles analysis of radiative recombination in lead-halide perovskites, ACS Energy Lett. 3 (2018) 2329–2334.
[42] S.E. Guo, Z.P. Deng, M.X. Li, B.J. Jiang, C.G. Tian, Q.J. Pan, H.G. Fu, Phosphorus-doped carbon nitride tubes with a layered micronanostructure for enhanced visible-light photocatalytic hydrogen evolution, Angew. Chem. 128 (2016) 1862–1866.
[43] W.L. Zhen, X.F. Ning, B.J. Yang, Y.Q. Wu, Z. Li, G.X. Lu, The enhancement of CdS photocatalytic activity for water splitting via anti-photocorrosion by coating Ni_2P shell and removing nascent formed oxygen with artificial gill, Appl. Catal. B Environ. 221 (2018) 243–257.
[44] M.L. Lv, G. Liu, X.X. Xu, Homologous compounds $Zn_nIn_2O_{3+n}$ (n = 4, 5, and 7) containing laminated functional groups as efficient photocatalysts for hydrogen production, ACS Appl. Mater. Interfaces 8 (2016) 28700–28708.
[45] H. Pang, X.G. Meng, P. Li, K. Chang, W. Zhou, X. Wang, X.L. Zhang, W. Jevasuwan, N. Fukata, D.F. Wang, J.H. Ye, Cation vacancy-initiated CO_2 photoreduction over ZnS for efficient formate production, ACS Energy Lett. 4 (2019) 1387–1393.
[46] Y.X. Pan, Y. You, S. Xin, Y.T. Li, G.T. Fu, Z.M. Cui, Y.L. Men, F.H. Cao, S.H. Yu, J.B. Goodenough, Photocatalytic CO_2 reduction by carbon-coated indium-oxide nanobelts, J. Am. Chem. Soc. 139 (2017) 4123–4129.
[47] S. Gao, B.C. Gu, X.C. Jiao, Y.F. Sun, X.L. Zu, F. Yang, W.G. Zhu, C.M. Wang, Z.M. Feng, B.J. Ye, Y. Xie, Highly efficient and exceptionally durable CO_2 photoreduction to methanol over freestanding defective single-unit-cell bismuth vanadate layers, J. Am. Chem. Soc. 139 (2017) 3438–3445.
[48] L. Zhang, W.Z. Wang, D. Jiang, E.P. Gao, S.M. Sun, Photoreduction of CO_2 on BiOCl nanoplates with the assistance of photoinduced oxygen vacancies, Nano Res. 8 (2015) 821–831.
[49] C. Zeng, Y.M. Hu, Hydrothermal synthesis of a $CoIn_2S_4$/g-C_3N_4 heterojunctional photocatalyst with enhanced photocatalytic H_2 evolution activity under visible light illumination, Nanotechnology 31 (2020) 505711.